Journal of Materials Chemistry A

PAPER

View Article Online
View Journal | View Issue

Cite this: J. Mater. Chem. A, 2018, 6, 15640

A and B site doping of a phonon-glass perovskite oxide thermoelectric†

L. M. Daniels, [a] S. Ling, [b] S. N. Savvin,[a] M. J. Pitcher, [a] M. S. Dyer, [a] J. B. Claridge,[a] B. Slater, [b] F. Corà,[b] J. Alaria *[c] and M. J. Rosseinsky *[a]

By tuning the A site cation size it is possible to control the degree of octahedral distortion and ultimately structural symmetry in the new perovskite solid solution $La_{0.5}Na_{0.5-x}K_xTiO_3$, affording a rhombohedral-to-cubic transition as x increases above 0.4. The La^{3+} and K^+ cations are distributed randomly across the A site leading to significant phonon disorder in cubic $La_{0.5}K_{0.5}TiO_3$ ($Pm\bar{3}m$) which produces a phonon-glass with a thermal conductivity of 2.37(12) W m^{-1} K^{-1} at 300 K; a reduction of 75% when compared with isostructural $SrTiO_3$. This simple cation substitution of Sr^{2+} for La^{3+} and K^+ maintains the flexible structural chemistry of the perovskite structure and two mechanisms of doping for the introduction of electronic charge carriers are explored; A site doping in $La_{1-y}K_yTiO_3$ or B site doping in $La_{0.5}K_{0.5}Ti_{1-z}Nb_zO_3$. The phonon-glass thermal conductivity of $La_{0.5}K_{0.5}TiO_3$ is retained upon doping through both of these mechanisms highlighting how the usually strongly coupled thermal and electronic transport can be minimised by mass disorder in perovskites. Precise control over octahedral distortion in A site doped $La_{1-y}K_yTiO_3$, which has rhombohedral ($R\bar{3}c$) symmetry affords lower band dispersions and increased carrier effective masses over those achieved in B site doped $La_{0.5}K_{0.5}Ti_{1-z}Nb_zO_3$ which maintains the cubic ($Pm\bar{3}m$) symmetry of the undoped $La_{0.5}K_{0.5}TiO_3$ parent. The higher Seebeck coefficients of A site doped $La_{1-y}K_yTiO_3$ yield larger power factors and lead to increased thermoelectric figures of merit and improved conversion efficiencies compared with the mechanism for B site doping.

Received 23rd April 2018
Accepted 20th June 2018

DOI: 10.1039/c8ta03739f

rsc.li/materials-a

Introduction

Thermoelectric devices convert heat energy directly into electricity or *vice versa* and have been utilised heavily as power sources for spacecraft and in thermoelectric heating or cooling technologies.[1,2] The most important application of these devices is to the recovery of waste heat energy, particularly in the industrial, residential and automotive sectors in order to improve efficiency and sustainability.[3,4] The performance of thermoelectric materials is assessed *via* the thermoelectric figure of merit $ZT = (S^2\sigma/\kappa)T$ comprised of the electronic conductivity (σ) and Seebeck coefficient (S), which together form the power factor ($S^2\sigma$), and the thermal conductivity (κ). Optimisation of ZT is made difficult by the complex coupled relationships that exist between each of the above properties. The phonon-glass electron-crystal (PGEC) approach envisages the decoupling of σ and S, which are typically governed by the electronic Boltzmann transport equation, from κ which is governed by phonon transport within the lattice.[5] "Phonon-glass" refers to the lattice contribution to the thermal conductivity (κ_{latt}) being minimised such that heat transport in a material is hindered like in a glass, while "electron-crystal" corresponds to the retention of a high σ and S within the same material leading to charge transport like in a semiconductor. These characteristics are widely reported in intermetallic systems such as clathrates and skutterudites,[6,7] which rely on the inclusion of rattler guest atoms within large structural cages to suppress κ_{latt} while electronic transport mediated through the covalent framework remains unaffected. The PGEC concept has been recently extended to oxide thermoelectrics.[8]

Metal oxides offer increased stability at high operating temperatures (automotive exhaust waste heat recovery typical operation temperature is 350–700 K, and industrial furnace waste heat recovery at 700–1100 K)[4,9] as well as higher natural abundance and lower toxicity of the constituent elements, leading to much lower costs and smaller environmental impacts when compared with the intermetallics used currently.[10,11] Titanate-based thermoelectrics, such as donor doped $SrTiO_3$, are the current state-of-the-art n-type thermoelectric oxides with a recent report of $ZT \approx 0.6$ at 1000 K which was achieved through nanoscale modulation of $SrTiO_3$ and TiO_2 inclusions in $Sr_{0.9}La_{0.1}Ti_{0.9}Nb_{0.1}O_3$.[12] The unique band

[a]Department of Chemistry, University of Liverpool, Crown Street, Liverpool, L69 7ZD, UK. E-mail: m.j.rosseinsky@liverpool.ac.uk

[b]Department of Chemistry, University College London, Gower Street, London, WC1E 6BT, UK

[c]Department of Physics, University of Liverpool, Oxford Street, Liverpool, L69 7ZE, UK. E-mail: jonathan.alaria@liverpool.ac.uk

† Electronic supplementary information (ESI) available. See DOI: 10.1039/c8ta03739f

structure of $SrTiO_3$ with contributions from both heavy and light carriers at the Fermi level,[13] gives rise to high power factors of 28–36 mW K^{-2} cm^{-1} at 300 K for $x = 0.015$–0.1 in $Sr_{1-x}La_xTiO_{3-\delta}$ single crystals but *ZT* is limited to 0.09 due to the large κ of 9–12 W m^{-1} K^{-1} in these materials.[14,15] With κ_{latt} contributing 75–100% of the total thermal conductivity, control over lattice phonon transport would allow for much higher figures of merit to be achieved in titanate perovskite thermoelectrics. $SrTiO_3$ can be considered as a phonon crystal where heat transport is mediated by coherent and long-distance propagation of phonons through the lattice, but due to the relatively small phonon mean free path (2–3 nm) the effects of nanostructuring approaches that are widely used to reduce κ in intermetallic thermoelectrics are negated unless nanometre-sized grains are achieved.[16] We highlighted previously the effectiveness of targeting a low κ that is intrinsic to the material, as opposed to originating from extrinsic microstructural effects, by exploiting the flexibility of the perovskite structure in a simple A site cation substitution that lead to a phonon-glass κ of $\approx$2.2 W m^{-1} K^{-1} in crystalline $La_{0.5}Na_{0.5}TiO_3$.[8] Through a combined experimental and computational approach, the origin of this glass-like behaviour was explained by increased phonon scattering as a result of charge and mass disorder resulting from the random distribution of La^{3+} and Na^+. Specifically, compared against $SrTiO_3$ the disordered cations in $La_{0.5}Na_{0.5}TiO_3$ act as locally decoupled oscillators with a broad range of vibrational frequencies which ultimately lead to phonon interactions being far more localised and heat transport being much less coherent. By achieving this intrinsically low κ, it enabled the emergence of PGEC properties where thermal and electronic transport are decoupled and could be altered independently.

The unique band dispersions observed in $SrTiO_3$ that allow for high power factors are correlated significantly with the high symmetry of the cubic structure and linearity of the Ti–O–Ti bonding.[13] $La_{0.5}Na_{0.5}TiO_3$ is a rhombohedrally-distorted perovskite with an $\approx 8^\circ$ tilt of the TiO_6 octahedra and non-linear Ti–O–Ti bond angles of $\approx 167^\circ$.[8,17] This tilting decreases overlap interactions between the Ti 3d and O 2p orbitals that are responsible for the dispersion of the valence and conduction bands in $SrTiO_3$, which decreases band dispersion thus increasing the charge carrier effective mass and in turn reducing the electronic conductivity. Symmetry considerations indicate that band dispersions are highest in the cubic perovskite phase, leading to the highest conductivity.[8,13] It is a widely accepted feature of the perovskite structure that it is possible to influence the symmetry of the material by tuning the cation size, and the effect of this can be estimated through the Goldschmidt tolerance factor, $t = (r_A + r_O)/\sqrt{2}(r_B + r_O)$, where the highest symmetry cubic structures have values closest to unity.[18,19] By increasing the cation size on the A site of $La_{0.5}Na_{0.5}TiO_3$ through substitution of Na^+ for K^+ ($r_{Na^+} = 1.39$ Å and $r_{K^+} = 1.64$ Å)[20] in $La_{0.5}Na_{0.5-x}K_xTiO_3$, *t* can be increased from 0.98 closer to 1. This is a new solid solution that is not reported in the literature and very little information is available on the fully substituted end-member phase $La_{0.5}K_{0.5}TiO_3$. This phase has been prepared previously through hydrothermal,[21] and high-pressure synthesis,[22] however detailed analysis and understanding of the structures is lacking. A cubic structure was reported by Brous *et al.*,[23] however this was based on a non-stoichiometric composition of $La_{0.531}K_{0.469}TiO_3$. We report the ceramic ambient pressure synthesis and detailed study of $La_{0.5}K_{0.5}TiO_3$ and the new perovskite solid solution $La_{0.5}Na_{0.5-x}K_xTiO_3$. Through crystal structure engineering and tuning of A site cation size it is possible to obtain cubic symmetry leading to band dispersions optimised for maximum conductivity in the perovskite $La_{0.5}K_{0.5}TiO_3$ while retaining the A site disorder that suppresses κ and leads to phonon-glass behaviour. The chemical flexibility of this material is demonstrated by donor doping on either the A or B site giving rise to electronic transport and power factors comparable to other doped titanate perovskites while the thermal conductivity remains mostly unaffected.

Experimental

Synthesis and processing of $La_{0.5}Na_{0.5-x}K_xTiO_3$

Pre-dried reagents of La_2O_3 (99.99%, Aldrich), Na_2CO_3 (99.997%, Alfa Aesar), K_2CO_3 (99.997%, Alfa Aesar) and TiO_2 (99.99%, Aldrich) were weighed out on a $\approx$1.7 gram scale to give desired compositions. All reagents were dried overnight at 473 K before weighing, except for La_2O_3 which was annealed at 1223 K. The powder mixtures were ground in acetone for 10 minutes before being fired as a powder in air at 1273 K for 4 hours placed in an alumina crucible. Heating and cooling rates were 1 and 5 K min^{-1}, respectively. The fired powders were ground for 10 minutes before being pressed uniaxially into a 13 mm pellet approximately 1 gram in mass. A portion of the powder was kept separate ($\approx$0.7 grams) to be used as sacrificial mixture in order to minimise the loss of volatile Na_2O and K_2O species during sintering. The pellet was then further pressed under an isostatic pressure of 200 MPa at ambient temperature using an Autoclave Engineers Cold Isostatic Press. These cold-pressed pellets were placed in an alumina boat and buried in the sacrificial powder before being sintered for 8 hours at 1623 K in air using heating and cooling rates of 1 and 3 K min^{-1}, respectively.

Synthesis and processing of $La_{1-y}K_yTiO_3$ and $La_{0.5}K_{0.5}Ti_{1-z}Nb_zO_3$

Preparation of powder mixtures for the doped materials was done using a procedure similar to that described above for $La_{0.5}Na_{0.5-x}K_xTiO_3$. Nb_2O_5 (99.9985%, Alfa Aesar) was used for the B site doped compositions. The sintering step performed at 1623 K for 8 hours, with the cold-pressed pellet buried under sacrificial powder of the same composition, was done under a 50 mL min^{-1} flow of H_2/N_2 (5/95%) instead of air in order to reduce the sample. To ensure the processing conditions were consistent for each composition, the $p(O_2)$ was monitored during each reduction step using a Cambridge Sensotec Rapidox 2100 Oxygen Analyser. The furnace was purged with flowing H_2/N_2 (5/95%) to achieve a $p(O_2)$ of 10^{-19} ppm before the pellets were sintered.

Pairs of pellets for each composition were processed in the same reactions; one pellet for the measurement of thermal

transport, and the other for measurement of electronic transport. Pellet densities were determined using the Archimedes method.

Characterisation

Structural analyses of the new $La_{0.5}Na_{0.5-x}K_xTiO_3$, $La_{1-y}K_yTiO_3$ and $La_{0.5}K_{0.5}Ti_{1-z}Nb_zO_3$ materials were performed through Rietveld analysis of synchrotron X-ray powder diffraction (SXRD) data and powder neutron diffraction (PND) data. SXRD data were recorded at beamline I11 ($\lambda = 0.82608$ Å) at Diamond Light Source, U.K, with the powders contained within 0.3 mm diameter borosilicate capillaries. PND data were collected on HRPD at ISIS, the U.K. time-of-flight spallation neutron source, with the powders loaded into thin-walled cylindrical vanadium cans of 8 mm diameter. Data were measured at ambient conditions on detector banks 1 ($2\theta = 168°$), 2 ($2\theta = 90°$) and 3 ($2\theta = 30°$) and were corrected for absorption effects before analysis. Rietveld refinements were carried out using Topas Academic.[24] SEM images were collected using a Hitachi S-4800, cold cathode, field-emission scanning electron microscope (SEM) from pellets that were deposited on a carbon tape attached to an aluminium stub.

Elemental analysis

Analysis of sample compositions was undertaken using Inductively Coupled Plasma Optical Emission Spectrometry (ICP-OES). Solutions of $La_{1-y}K_yTiO_3$ ($y = 0.5$, 0.45 and 0.4) and $La_{0.5}K_{0.5}Ti_{1-z}Nb_zO_3$ ($z = 0.05$ and 0.1) were prepared through acid digestion of approximately 10 mg pieces of sintered pellet. These were dissolved in 7 mL of concentrated HCl sealed inside Teflon-lined stainless-steel Parr autoclaves which were heated to 503 K for 4 hours. These solutions were made up to 100 mL in volumetric glassware using ultra-pure water. Metal contents were corrected for interference by comparing separate and combined metal solutions of known concentrations. Data were collected on an Agilent 5110 SCDV ICP-OES instrument.

Measurement of thermal conductivity

Thermal diffusivity (α) data were measured by laser flash analysis using a Netzsch LFA 457. The polished pellets (approximately 10 mm in diameter and 1.5–2 mm thick) were coated in colloidal graphitic carbon before being placed inside the sample chamber which was evacuated and purged three times before being put under a constant helium flow of 100 mL min^{-1}. Data were collected in 50 K steps in the temperature range 298 to 943 K, with a five minute equilibration at each temperature. Three measurements were recorded at each temperature and averaged and the standard deviation of these points was typically below 0.5%. Thermal expansion profiles were measured on a Netzsch DIL 402C push-rod dilatometer under dynamic vacuum on bars approximately 4 mm in length. Continuous measurements were made from 298 to 973 K with a heating rate of 3 K min^{-1}. Errors on dilatometry measurements are assumed to be 5% as informed by the manufacturer. Heat flux profiles were measured on small pieces of sintered pellet ($\approx$50 mg) using a Netzsch DSC 404 F1 differential scanning calorimeter under a 50 mL min^{-1} flow of helium. Data were recorded from 323 to 973 K at a heating rate of 10 K min^{-1}. Data were also measured under identical conditions from a sapphire standard (also 50 mg) which was used to determine the heat capacities (C_p) of each sample. Errors on heat capacities were assumed to be 5% as advised by the manufacturer. The thermal conductivity (κ) was calculated by combining the diffusivity, dilatometry and heat capacity data through $\kappa(T) = \alpha(T)C_p(T)\rho(T)$ where ρ is the pellet density. The total thermal conductivity (κ) is equal to the sum of the lattice (κ_{latt}) and electronic (κ_{elec}) contributions through $\kappa = \kappa_{latt} + \kappa_{elec}$. The electronic contribution to the thermal conductivity is estimated through the Wiedemann–Franz law which states $\kappa_{elec} = LT\sigma$, where L is the Sommerfield value for the Lorenz number (2.45×10^{-8} W Ω K^{-2}), T is the temperature and σ is the electronic conductivity.[25]

Measurement of electronic conductivity and Seebeck coefficient

Simultaneous electronic conductivity (σ) and Seebeck coefficient (S) measurements were made on an Ulvac-Riko ZEM-3 instrument from rectangular bars (dimensions of 2 × 2 × 8 mm) which were cut from sintered pellets using a low-speed diamond-blade saw. The bars were mounted in a 4-point geometry with outer current electrodes in contact with each end face and inner thermocouple and voltage probes pressed against one of the longer (8 mm) sides of the bar. The sample chamber was evacuated and purged three times with helium and then dosed with 0.01 MPa of helium before commencing measurement. Data were recorded at 50 K intervals from 323 to 973 K, applying 10, 20 and 30 K temperature gradients to the bar at each temperature step. Errors on both σ and S were assumed to be 5% on advice of the manufacturer.

Phonon calculations

To achieve a better understanding of the atomistic origin of the different thermal conductivities of $La_{0.5}K_{0.5}TO_3$ and $SrTiO_3$, accurate first principles calculations were performed. All phonon calculations of $La_{0.5}K_{0.5}TO_3$ (with random La/K distribution) and $SrTiO_3$ were performed in the harmonic approximation using the code CP2K, at the density functional theory (DFT)/PBE level of theory.[26,27] CP2K employs a mixed Gaussian/plane-wave basis set; in the current study, a double-ζ plus polarization quality Gaussian basis set,[28] and a 400 Ry plane-wave cutoff for the auxiliary grid were employed in conjunction with Goedecker–Teter–Hutter pseudopotentials.[29,30] A convergence threshold of 1.0×10^{-8} Ha was used for the self-consistent field cycle, and structural optimizations were considered to have converged when the maximum force on all atoms fell below 1.0×10^{-4} Ha per Bohr. All calculations were performed with the Γ-point approximation, using a rhombohedral supercell containing 640 atoms (lattice constants $\sim$ 22 Å). The second derivatives of the total energy with respect to the atomic displacements were computed numerically, from analytical first derivatives, using atomic displacements of 0.01 Bohr from the equilibrium position. Normal modes and

frequencies were obtained by diagonalization of the dynamical matrix. To understand the nature of phonon modes in $La_{0.5}K_{0.5}TiO_3$, the mean distance between the 10 atoms that participate to the greatest extent in a given phonon mode as defined by their displacement amplitudes were calculated, denoted as $d_{average}$, which quantifies the localisation of phonon modes and is given by:

$$d_{average} = \frac{1}{n}\sum_{i,j} d_{ij} \quad (1)$$

where i and j are indices of the atoms with the largest displacement amplitudes for the normal mode considered, d_{ij} is their interatomic distance (using minimum image convention), and n is the number of pairs of atoms.

Electronic band structure calculations

To understand how the octahedral tilting (as present in $La_{0.5}Na_{0.5-x}K_xTiO_3$ for $x < 0.4$) modifies the band dispersions at the bottom of the conduction band, which may directly affect the thermoelectric power factor, we have performed additional DFT calculations on the electronic band structures of $SrTiO_3$, taking it as a model system, and we consider different amounts of octahedral tilting. All electronic band structure calculations of $SrTiO_3$ were performed using CRYSTAL14 at DFT/PBE0 level of theory.[31,32] Reciprocal space sampling has been performed for all structures using a Monkhorst–Pack grid of $8 \times 8 \times 8$ k-points. Standard all electron basis sets from the CRYSTAL online database (https//:www.crystal.unito.it) have been used for O and Ti (indicated by the following labels online: O_8−411d11G_valenzano_2006, Ti_86-411(d31) G_darco_unpub). For Sr, we have used a small-core relativistic effective core potential with a double-zeta quality valence basis set (indicated by Sr_m-S-RSC_Heyd_2005_Heyd_2005 online). The initial structure of cubic $SrTiO_3$ in the rhombohedral cell (space group $R\bar{3}c$) without any octahedral tilting has been fully optimised, which was then used as the starting point to generate $SrTiO_3$ structures with octahedral tilting. The two $SrTiO_3$ structures with different amounts of octahedral tilting were manually generated, by adjusting the oxygen fractional coordinates and lattice parameters, to ensure Ti–O bond lengths remain the same. Subsequent band structure calculations were performed for the unoptimized structures (for $SrTiO_3$ with octahedral tilting).

Results and discussion

Phonon-glass thermal conductivity in $La_{0.5}Na_{0.5-x}K_xTiO_3$

$La_{0.5}Na_{0.5}TiO_3$ has a rhombohedral ($R\bar{3}c$) perovskite structure, described by a tilting of the TiO_6 octahedra about the [111] direction of the primitive cubic cell ($\bar{a}\bar{a}\bar{a}$ tilt system in Glazer's notation),[33] and disordered A site cation distribution. Phonon calculations that previously highlighted the localisation of vibrational modes in $La_{0.5}Na_{0.5}TiO_3$ were performed for $La_{0.5}K_{0.5}TiO_3$. Calculation of $d_{average}$, which corresponds to the average separation between the ten atoms with largest phonon displacement amplitudes for each individual phonon mode is shown in Fig. 1 for $SrTiO_3$ and $La_{0.5}K_{0.5}TiO_3$. The results show that $La_{0.5}K_{0.5}TiO_3$ has similarly promising features to those observed in $La_{0.5}Na_{0.5}TiO_3$,[8] indicating that the disordered distribution of La^{3+} and K^+ leads to significant phonon localisation and should yield a phonon-glass thermal conductivity similar to $La_{0.5}Na_{0.5}TiO_3$. Compared against $SrTiO_3$ which has a $d_{average}$ of $\approx$11 Å across the entire phonon spectrum, $d_{average}$ is reduced by 15–20% in $La_{0.5}K_{0.5}TiO_3$. We also showed previously how the coexisting dispersive and dispersion-less bands at the bottom of the conduction band that allow for high power factors in cubic $SrTiO_3$ are retained in rhombohedral $La_{0.5}Na_{0.5}TiO_3$. Table 1 shows relative effective masses (m^*) extracted from the calculated electronic band structures of $SrTiO_3$ at different octahedral tilt angles. The effective masses decrease with decreasing tilt angle for both bands, which shows that a cubic zero-tilt structure provides band dispersions that are optimised for highly mobile carriers towards the best possible electronic conductivity. From these computational indications, $La_{0.5}K_{0.5}TiO_3$ presents a suitable low thermal conductivity target with band dispersions optimised for electronic conductivity and the structural flexibility of a perovskite to allow for carrier doping.

Potassium was substituted for sodium through the new solid solution $La_{0.5}Na_{0.5-x}K_xTiO_3$. The results of Rietveld refinement against SXRD and PND data measured on $La_{0.5}K_{0.5}TiO_3$, prepared at 1300 °C through solid state synthesis, are shown in Fig. 2. The single phase powder diffraction pattern for $La_{0.5}K_{0.5}TiO_3$ can be indexed to a cubic unit cell with space group symmetry $Pm\bar{3}m$ and lattice parameter of 3.908212(5) Å. This is slightly larger than the only reported lattice parameter of 3.907 Å,[23] which was based on a composition of $La_{0.531}K_{0.469}TiO_3$ implying that more of the larger K^+ is present in the structure reported here as evidenced by the refined occupancies (Table S1, ESI†) and presents the first structural analysis of stoichiometric $La_{0.5}K_{0.5}TiO_3$. The La^{3+} and K^+ are modelled on the 1a crystallographic position and both A and B sites are modelled using

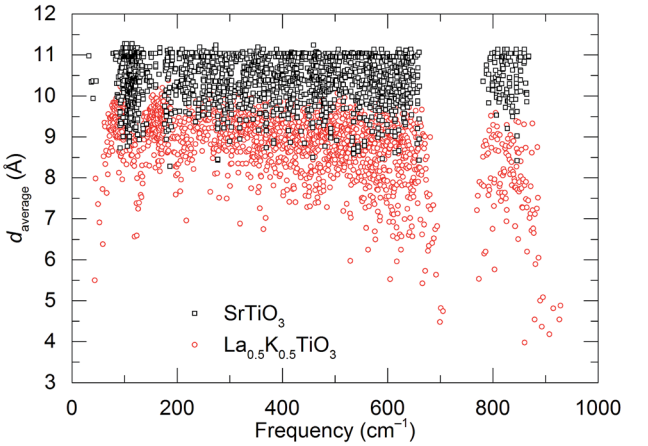

Fig. 1 Phonon localisation in $La_{0.5}K_{0.5}TiO_3$ (red circles) determined from DFT calculations compared against interactions in the phonon-crystal $SrTiO_3$ (black squares). The parameter $d_{average}$ is calculated for individual phonon modes as the mean distance between the ten atoms that participate to the greatest extent in that phonon mode as defined by their displacement amplitudes.

Table 1 Effective masses (m^*) for the flat and two dispersive bands along gamma–kappa direction extracted from hybrid DFT calculations at different tilt angles in $SrTiO_3$. The effective masses are normalised to the effective mass of the dispersive bands in the cubic structure without octahedral tilting

Tilt angle (°)	m^*_{flat}	$m^*_{dispersive}$	$m^*_{flat}/m^*_{dispersive}$
0.00	6.14	1.00/1.00	6.14/6.14
3.25	8.07	1.02/0.99	7.89/8.13
6.50	14.05	1.14/1.05	12.37/13.35

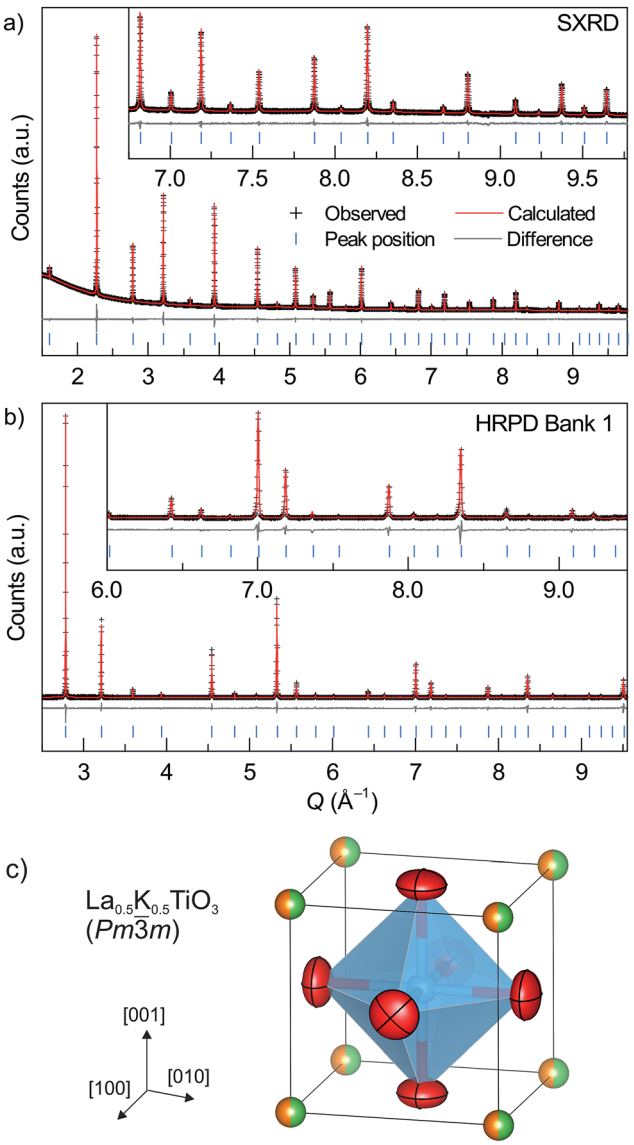

Fig. 2 Rietveld refinements against (a) SXRD (λ = 0.82608 Å) and (b) high resolution NPD data measured on bank 1 (backscattering 2θ = 168°) of HRPD at room temperature for $La_{0.5}K_{0.5}TiO_3$. The refinement model is based on cubic $Pm\bar{3}m$ symmetry with A site metals La^{3+} and K^+ modelled on the 1*a* (0, 0, 0) position, the Ti^{4+} on the 1*b* (1/2, 1/2, 1/2) position and oxide ions on the 3*c* positions (0, 1/2, 1/2). The cubic cell of $La_{0.5}K_{0.5}TiO_3$ is shown in (c) with anisotropic displacement ellipsoids for the oxide positions.

isotropic displacement parameters (Table S1, Fig. S1, ESI†). The use of anisotropic displacement parameters (ADPs) to model the 3*c* oxygen position yielded a small improvement to the fit, decreasing R_{wp} from 1.525% to 1.485%. This gave a similar equivalent U_{iso} (0.01446(16) Å^2) to modelling the site using isotropic displacement parameters (0.01425(7) Å^2) but resulted in slightly elongated ADPs displaying atomic motion perpendicular to the Ti–O–Ti direction as is expected due to thermally induced rotational motion of the BO_6 octahedra.

A rhombohedral-to-cubic transition exists within the $La_{0.5}Na_{0.5-x}K_xTiO_3$ series and occurs upon increasing x between 0.4 and 0.5 with $La_{0.5}K_{0.5}TiO_3$ being cubic ($Pm\bar{3}m$), and compositions of $0.1 < x < 0.4$ being indexed to the same rhombohedral unit cell as $La_{0.5}Na_{0.5}TiO_3$ ($R\bar{3}c$). This rhombohedral-to-cubic transition that occurs between $x = 0.4$ and 0.5 is not immediately obvious upon examination of the c/a lattice parameter ratio shown in Fig. 3a which suggests that the unit cell becomes metrically cubic at $x = 0.2$ (where $c/a = \sqrt{6} = 2.4495$), and not at $x = 0.5$. Only full structural analysis through Rietveld refinement can confirm that the rhombohedral structure, defined by the symmetry elements present, persists in the $0.1 < x < 0.4$ compositions and that cubic symmetry is achieved only for $x = 0.5$. The primitive pseudocubic cell volume increases linearly towards $x = 0.5$ as shown in Fig. 3a. The replacement of smaller sodium with larger potassium (r_{Na^+} = 1.39 Å and r_{K^+} = 1.64 Å)[20] increases the average cation size on the A site and causes an expansion of the unit cell. This expansion of the unit cell with increasing x results in a linear decrease in the octahedral tilt angle, ϕ, which is used to describe the rotation of the BO_6 octahedra about the threefold axis of the primitive cubic cell and is determined from the convention of Megaw, $\phi = \arctan[2\sqrt{3}(x - 0.5)]$, where x is the positional parameter of the 18*e* oxygen site.[34] Fig. 3b shows how the octahedral tilt angle decreases from 7.9142(2)° for $x = 0$ to 0° for $x = 0.5$ in $La_{0.5}Na_{0.5-x}K_xTiO_3$, with the rhombohedral-to-cubic transition between tilted and non-tilted structures occurring between $x = 0.4$ and 0.5. Alternatively, this can be viewed through the Ti–O–Ti bond angles which become more linear with x, increasing from 167.044(14)° for $x = 0$ to 180° in $x = 0.5$. While ϕ is decreasing towards 0° with increasing x, there is a simultaneous distortion of the octahedra themselves where O–Ti–O angles deviate away from the ideal 90° and can be quantified by the octahedral bond angle variance in eqn (2)[35]

$$\sigma^2 = \frac{1}{n-1}\sum_{i}^{n}(\theta_i - \theta_0)^2 \quad (2)$$

where n is the number of bonds while θ_i and θ_0 denote the i^{th} and ideal bond angles of the octahedron, respectively. This is shown to decrease in Fig. 3b as a function of increasing x, reaching zero at $x = 0.5$ indicating ideal 90° O–Ti–O angles are achieved in $La_{0.5}K_{0.5}TiO_3$. Although it is not fully understood, it is evident that this competition between simultaneous octahedral tilting (ϕ) and octahedral distortion (σ^2) in $La_{0.5}Na_{0.5-x}K_xTiO_3$ leads to the compositions of $0.2 < x < 0.4$ adopting metrically cubic unit cells. Fig. 3c shows that the separate A–O distances converge at $x = 0.5$ with the average A–O distance increasing

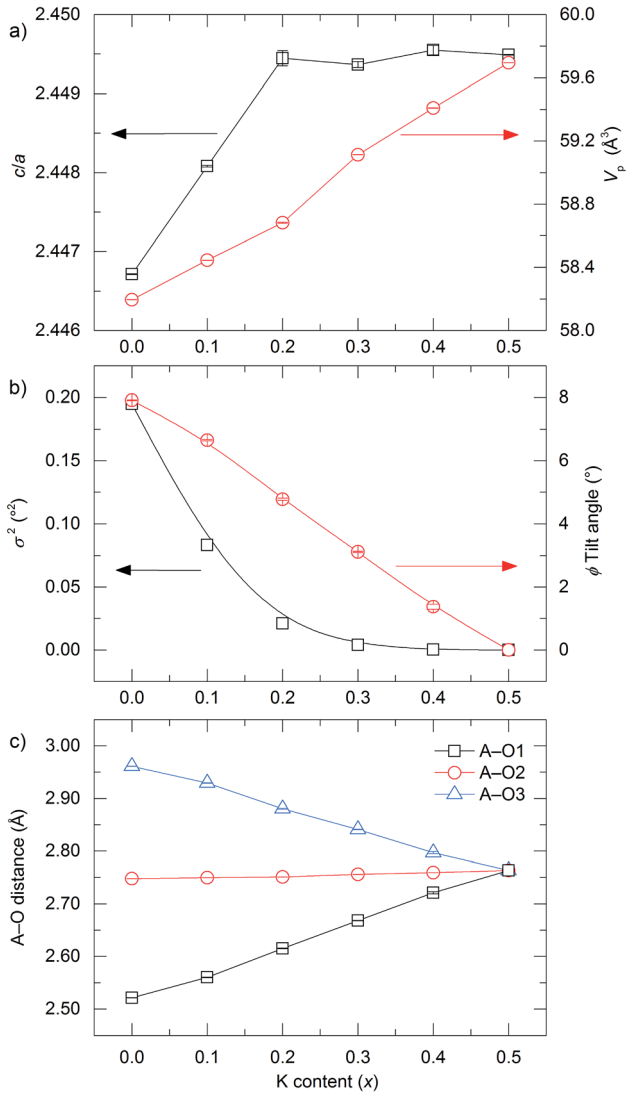

Fig. 3 Variation in (a) c/a lattice parameter ratio (black squares) and primitive pseudocubic cell volume (red circles), (b) bond angle variance (black squares) and octahedral tilt angle (red circles), and (c) A–O distances as a function of x in the solid solution $La_{0.5}Na_{0.5-x}K_xTiO_3$ refined from SXRD and high resolution NPD data. Primitive cell parameters are obtained through $a_p = a/\sqrt{2}$ and $c_p = c/2\sqrt{3}$. Octahedral tilt angles (ϕ) are determined through $\phi = \arctan[2\sqrt{3}(x - 0.5)]$, where x is the x coordinate of the 18e oxide position in space group $R\bar{3}c$. Bond angle variance is obtained from eqn (2) in the text.

following the expansion of the A site cations and unit cell. The A–O/B–O ratio increases with x towards the value of $\sqrt{2}$ (Table S4, ESI†) which relates these distances in the cubic perovskite structure. The cubic structure of $La_{0.5}K_{0.5}TiO_3$ is very similar to that of $SrTiO_3$ with comparable lattice parameters of a = 3.908212(5) Å and 3.909149(3) Å, respectively.[36] Refinement of ADPs to model the 18e oxygen positions in rhombohedral $La_{0.5}Na_{0.2}K_{0.3}TiO_3$ gave similar results to those in cubic $La_{0.5}K_{0.5}TiO_3$ where their positions were elongated normal to the central atom of the octahedron and along the direction of octahedral rotation (Fig. S1, ESI†). The symmetry of space group $R\bar{3}c$ allows for refinement of ADPs for the A site, which results in a slight elongation of the position along the c axis of the unit cell towards neighbouring octahedra (Fig. S1, ESI†). Despite the static disorder generated by three different cations occupying the A site, the local deviation away from the average structure is minimal with a root mean square displacement of 0.107(16) Å at 300 K. Most importantly, the structural analysis of the $La_{0.5}Na_{0.5-x}K_xTiO_3$ solid solution and of $La_{0.5}K_{0.5}TiO_3$ in particular, shows that the La^{3+} and K^+ are disordered across the twelve-coordinate A site. This disorder induced phonon-glass behaviour of the thermal conductivity in $La_{0.5}Na_{0.5}TiO_3$,[8] a property expected to be replicated in $La_{0.5}K_{0.5}TiO_3$ following the observation of phonon localisation (Fig. 1).

$La_{0.5}K_{0.5}TiO_3$ is a crystalline material that offers the high symmetry cubic structure of $SrTiO_3$, with the unique multi-carrier band structure suited towards thermoelectricity,[13] along with a disordered distribution of A site metals which have considerable mass contrast. The disorder scattering parameter is defined by $\Gamma = \Gamma_{MF} + \Gamma_{SF}$ and contributes significantly to phonon scattering in these materials. It combines contributions from the mass contrast of defects (Γ_{MF}) and the size strain (Γ_{SF}) induced by ionic radius variance of defects, both of which are effective disruptors of phonon transport within a crystal lattice.[37] The mass fluctuation and strain field terms are quantified through $\Gamma_{MF} = \sum_i f_i(1 - m_i/\bar{m})^2$ and $\Gamma_{SF} = \sum_i f_i(1 - r_i/\bar{r})^2$ respectively, where f_i is the fraction of atoms which have mass m_i and radius r_i occupying a crystallographic site with average mass $\bar{m}$ and average radius $\bar{r}$. Fig. 4a shows how Γ, Γ_{MF} and Γ_{SF} change as a function of x in $La_{0.5}Na_{0.5-x}K_xTiO_3$. Replacement of lighter sodium with heavier potassium results in Γ_{MF} decreasing from 0.513 for $x = 0$ to 0.314 for $x = 0.5$, while the increased size disparity between La^{3+} and K^+ raises Γ_{SF} from 1.19×10^{-4} to 8.71×10^{-3} for those respective values of x. Although Γ_{SF} is no longer negligible, with a 2.70% contribution to Γ in $La_{0.5}K_{0.5}TiO_3$ compared to 0.02% in $La_{0.5}Na_{0.5}TiO_3$, this increase in cation size variance is insufficient to alleviate the reduction in Γ_{MF} that remains the dominant contribution to the total Γ, which decreases from 0.513 to 0.323 between $x = 0$ and 0.5, respectively. The measured thermal conductivities across the $La_{0.5}Na_{0.5-x}K_xTiO_3$ series are shown in Fig. 4b (Fig. S4, ESI†). One of the more striking features of the experimental data is that the thermal conductivity of the compositions in $La_{0.5}Na_{0.5-x}K_xTiO_3$ are not significantly different despite the reduction in Γ shown in Fig. 4a. The compositions of $x = 0$, 0.3 and 0.5 in $La_{0.5}Na_{0.5-x}K_xTiO_3$ are electronically insulating meaning that κ is equal to κ_{latt} in these materials. The thermal conductivity of $La_{0.5}K_{0.5}TiO_3$ retains the phonon-glass characteristics that were observed for $La_{0.5}Na_{0.5}TiO_3$ where the temperature dependence of κ_{latt} matches that of the heat capacity. Additionally, both the magnitude and temperature dependence of κ_{latt} observed for $La_{0.5}K_{0.5}TiO_3$ are comparable with the theoretical minimum thermal conductivity (κ_{min}) that would be expected if $SrTiO_3$ exhibited phonon glass properties. This quantity, compared against experimental data in Fig. 4b, is estimated through Cahill's model for disordered crystalline solids described by eqn (3)

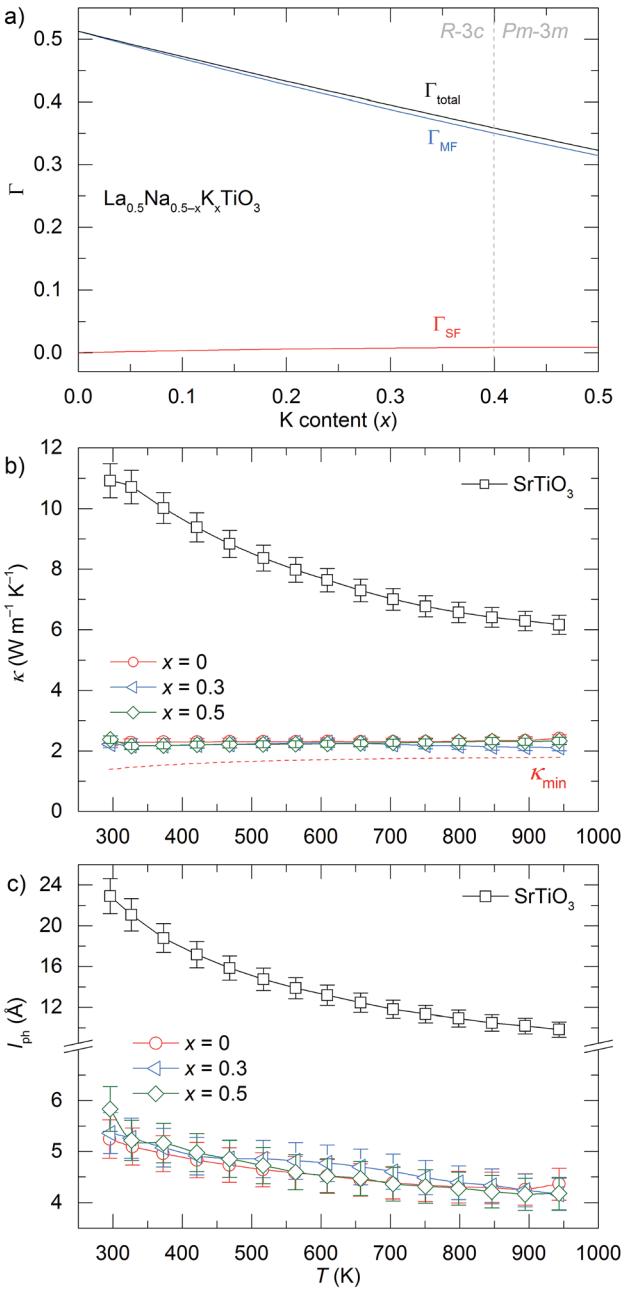

Fig. 4 Dependence of (a) disorder scattering parameter (Γ), including mass (Γ_{MF}) and size (Γ_{SF}) contributions shown in blue and red respectively, (b) thermal conductivity (κ), and (c) phonon mean free path (l_{ph}) on x in the solid solution $La_{0.5}Na_{0.5-x}K_xTiO_3$. The theoretical minimum thermal conductivity (κ_{min}) of $SrTiO_3$ is shown as the dashed line in (b) and is calculated from Cahill's model for disordered crystalline solids.[38] Phonon mean free paths in (c) are obtained through eqn (4) and (5).

$$\kappa_{min} = \left(\frac{\pi}{6}\right)^{\frac{1}{3}} k_B N^{\frac{2}{3}} \sum_i \nu_i \left(\frac{T}{\theta_i}\right)^2 \int_0^{\frac{\theta_i}{T}} \frac{x^3 e^x}{(e^x-1)^2} dx \quad (3)$$

where k_B is the Boltzmann constant, N is the number density of atoms known from structural refinement, ν_i is the velocity of sound and θ_i is used as the cut-off frequency.[38] Experimental values of transverse and longitudinal velocities of sound extracted from $SrTiO_3$ single crystals were used to calculate θ_i through eqn (4) and are listed in Table S5 (ESI†)[39]

$$\nu_s = \frac{k_B \theta_D}{\hbar \sqrt[3]{6\pi^2 N}} \quad (4)$$

The close comparison to κ_{min} and glass-like dependence of κ_{latt} with temperature shows that $La_{0.5}K_{0.5}TiO_3$ is a crystalline material with phonon glass thermal properties. The magnitude of κ_{latt} at room temperature increases from 2.28 to 2.40 W m^{-1} K^{-1} from $x = 0$ to 0.5 respectively, which is associated with the decrease in Γ. This is only a minor change in κ_{latt} in contrast to a considerable change to Γ, indicating that the disorder parameter has a smaller influence on the thermal conductivity in materials which display phonon-glass properties compared to those with phonon-crystal properties as was shown in $Sr_{1-x}La_{0.67x}\square_{0.33x}TiO_3$ where increasing Γ had a smaller effect as κ_{latt} approached κ_{min}.[40] The values of κ_{latt} observed for $La_{0.5}Na_{0.5-x}K_xTiO_3$ are very low when compared against both doped and undoped compositions of $SrTiO_3$ which exhibit κ_{latt} values in the range of 4–12 W m^{-1} K^{-1} at 300 K,[41,42] and perhaps most importantly exhibit a temperature dependence that is typical of a phonon-crystal where a T^{-1} relationship is observed at high temperatures due to the anharmonic interaction of phonon–phonon Umklapp scattering processes. Data measured from undoped $SrTiO_3$ is provided for comparison purposes in Fig. 4b and show that the substitution of both La^{3+} and K^+ for Sr^{2+} on the A site of the perovskite structure affords a 75% reduction in thermal conductivity at 300 K (2.37(12) W m^{-1} K^{-1} for $La_{0.5}K_{0.5}TiO_3$ compared against 10.91(56) W m^{-1} K^{-1} for $SrTiO_3$). This low, glass-like thermal conductivity observed experimentally for $La_{0.5}K_{0.5}TiO_3$ is consistent with the results obtained from calculations (Fig. 1) which showed that phonons are more localised in comparison with the phonon-crystal $SrTiO_3$. The calculations, performed at DFT level, show increased contributions to the phonon density of states (PDOS) in the low frequency region in comparison with $SrTiO_3$ (Fig. S5, ESI†). The largest contribution to the PDOS in $SrTiO_3$ is at $\approx$110 cm^{-1}, however two broader contributions are observed in this region for $La_{0.5}K_{0.5}TiO_3$; a peak at $\approx$95 cm^{-1} predominantly consisting of contributions from La, and a second peak at $\approx$170 cm^{-1} arising from the contributions of K and Ti. Through this combined experimental and computational understanding of phonon behaviour in $La_{0.5}K_{0.5}TiO_3$, it is clear the vibrational disorder introduced by having two high-mass contrast cations present on a single crystallographic position is highly effective at scattering phonons and reducing heat transport within the lattice, leading to the observed glass-like thermal conductivity in crystalline $La_{0.5}K_{0.5}TiO_3$. This increased localisation of phonons is similar to that observed in $La_{0.5}Na_{0.5}TiO_3$,[8] and shows that the disordered La^{3+} and K^+ cations in $La_{0.5}K_{0.5}TiO_3$ are responsible for the phonon-glass behaviour by acting as decoupled local oscillators with incoherent phases which dramatically reduce time and distance between phonon scattering events. Experimentally, this is evident from the phonon mean free paths that are shown in

Fig. 4c and are calculated from eqn (4) and (5) using θ_D of 630 K.[43]

$$\kappa_{latt} = \frac{1}{3} C_V l_{ph} \nu_s \quad (5)$$

where C_V is the isochoric heat capacity, and l_{ph} is the phonon mean free path. The phonon mean free paths of compositions in the $La_{0.5}Na_{0.5-x}K_xTiO_3$ series all show relatively flat temperature dependence in comparison with $SrTiO_3$ which is a clear indicator of the emergence of glassy characteristics in these materials. The magnitudes of l_{ph} in $La_{0.5}Na_{0.5-x}K_xTiO_3$ of 4–6 Å are comparable to those of vitreous materials such as SiO_2 which typically are around 5–7 Å.[44] Microstructure was shown to influence κ_{latt} and l_{ph} of $SrTiO_3$,[16] however, this required nanometre-sized grains. The effect of microstructure in $La_{0.5}K_{0.5}TiO_3$ materials is negligible due to the large disparity between l_{ph} and grain size, which are shown through SEM (Fig. S6, ESI†) to be much larger and of the order of 10–20 μm.

Introduction of electronic charge carriers into $La_{0.5}K_{0.5}TiO_3$

One of the more useful features resulting from the complete replacement of Sr^{2+} for a charge balanced mixture of La^{3+} and K^+ in $La_{0.5}K_{0.5}TiO_3$ is that the chemical and structural flexibility of the perovskite structure is maintained. Electron doping in $SrTiO_3$ involves the incorporation of an aliovalent cation with higher charge, such as Ln^{3+} on the A site or Nb^{5+} on the B site,[42,45,46] which through charge compensation mechanisms reduces a sufficient amount of Ti^{4+} to Ti^{3+} giving rise to electronic transport. Even though the A site in $La_{0.5}K_{0.5}TiO_3$ has a disordered cation arrangement, the flexible structural chemistry enables the introduction of electronic carriers through doping of either the A or B site. Incorporation of Nb^{5+} onto the B site through $La_{0.5}K_{0.5}Ti_{1-z}Nb_zO_3$ allows for the mechanisms that govern the thermal and electronic properties to be confined to the separate A and B sites of the perovskite structure, respectively, as was reported for PGEC $La_{0.5}Na_{0.5}Ti_{1-x}Nb_xO_3$.[8] Doping of the A site can be achieved by targeting non-stoichiometric compositions through $La_{1-y}K_yTiO_3$ (with $y < 0.5$). This maintains the mass contrast that affords the phonon-glass thermal conductivity, and usefully allows for the same nominal charge carrier concentrations as $La_{0.5}K_{0.5}Ti_{1-z}Nb_zO_3$ to be accessed by using smaller dopant amounts due to the nature of the dopant mechanisms which are described by Kröger–Vink notation in reaction eqn (6) and (7), where A and B refer to the site occupied.

For $La_{1-y}K_yTiO_3$:

$$\left(\frac{1}{2}\right)La_2O_3 + K_A^{\times} + 2Ti_{Ti}^{\times} \rightarrow \left(\frac{1}{2}\right)K_2O + La_A^{\cdot\cdot\cdot} + Ti_B^{'} + \left(\frac{1}{2}\right)O_2 \quad (6)$$

For $La_{0.5}K_{0.5}Ti_{1-z}Nb_zO_3$:

$$\left(\frac{1}{2}\right)Nb_2O_5 + 2Ti_{Ti}^{\times} \rightarrow TiO_2 + Ti_B^{'} + Nb_B^{\cdot} + \left(\frac{1}{4}\right)O_2 \quad (7)$$

Through solid state reaction performed at 1300 °C under a H_2/N_2 (5%) atmosphere, it is possible to produce phase pure samples of $La_{1-y}K_yTiO_3$ with $0.4 \leq y \leq 0.5$ and $La_{0.5}K_{0.5}Ti_{1-z}Nb_zO_3$ up to $z = 0.1$. These values define the limits of doping for each material under these particular synthetic conditions; decreasing y below 0.4 in $La_{1-y}K_yTiO_3$ results in the formation of $La_2Ti_2O_7$ impurities, while increasing z further than 0.1 yields $LaNbO_4$ as an impurity phase in $La_{0.5}K_{0.5}Ti_{1-z}Nb_zO_3$. The effects of A and B site doping upon the unit cell parameters of $La_{1-y}K_yTiO_3$ and $La_{0.5}K_{0.5}Ti_{1-z}Nb_zO_3$ are shown in Fig. 5a and b, respectively. A linear decrease in unit cell volume is observed as a function of La^{3+} content in $La_{1-y}K_yTiO_3$ associated with the larger K^+ cation being replaced with La^{3+} ($r_{K^+} = 1.64$ Å and $r_{La^{3+}} = 1.36$ Å).[20] Both $La_{1-y}K_yTiO_3$ compositions are indexed to rhombohedral $R\bar{3}c$ symmetry with separation of primitive cell parameters a_p and c_p, shown in Fig. 5a (Tables S6–S8, Fig. S7 and S8, ESI†). This distortion away from the cubic symmetry of the $La_{0.5}K_{0.5}TiO_3$ parent results from the decreasing average cation size on the A site, as well as an increasing cation size on the B site from the reduction of Ti^{4+} to Ti^{3+} ($r_{Ti^{4+}} = 0.605$ Å and $r_{Ti^{3+}} = 0.67$ Å); the tolerance factor can be reduced by decreasing r_A or increasing r_B. Contrary to this, the cubic symmetry of the $La_{0.5}K_{0.5}TiO_3$ parent is

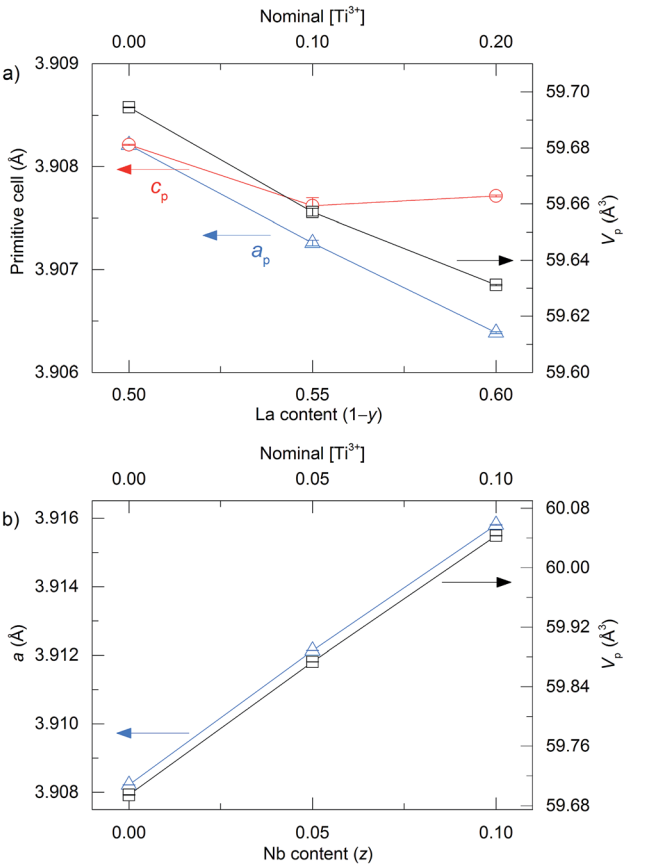

Fig. 5 Variation in (a) primitive unit cell parameters and volume as a function of La^{3+} content in A site doped $La_{1-y}K_yTiO_3$ with $R\bar{3}c$ symmetry, and (b) cubic unit cell parameter and volume in B site doped $La_{0.5}K_{0.5}Ti_{1-z}Nb_zO_3$ ($Pm\bar{3}m$) as a function Nb^{5+} substitution. The nominal Ti^{3+} concentrations are plotted on the top axes of each and increase with increasing La^{3+} and Nb^{5+} content. The $La_{0.5}K_{0.5}Ti_{1-z}Nb_zO_3$ series are cubic ($Pm\bar{3}m$), while $La_{1-y}K_yTiO_3$ materials are rhombohedral ($R\bar{3}c$).

maintained in the B site doped $La_{0.5}K_{0.5}Ti_{1-z}Nb_zO_3$ materials up to $z = 0.1$ with a linear increase in the unit cell parameter and volume shown in Fig. 5b (Tables S9–S11, Fig. S9 and S10, ESI†), consistent with the substitution of Ti^{4+} with larger Nb^{5+} ($r_{Ti^{4+}} = 0.605$ Å and $r_{Nb^{5+}} = 0.64$ Å). There remains no evidence for ordering of the A site cations even in non-stoichiometric $La_{1-y}K_yTiO_3$, indicating that the disordered distributions of La^{3+} and K^+, which we have shown to be essential for the phonon glass κ in these materials, are preserved in all materials reported in this study. The refined oxygen occupancies for the A and B doped materials studied through both SXRD and NPD did not provide any evidence for oxide deficiencies (Tables S7 and S10, ESI†). When refined, values within error of a fully occupied oxygen position were obtained much like the oxygen occupancies in the undoped materials $La_{0.5}K_{0.5}TiO_3$ and $La_{0.5}Na_{0.2}K_{0.3}TiO_3$ (Tables S1 and S2, ESI†).

The metal contents for each of the doped materials were determined using ICP-OES and are listed in Table 2. Both the La/K and Ti/Nb ratios agree very well with those from the nominal compositions, and compare closely to the refined occupancies obtained from Rietveld analysis of SXRD and PND data (Tables S1 and S6–S10, ESI†). The analysis shows near-stoichiometric ratios for La and K in the undoped $La_{0.5}K_{0.5}TiO_3$ parent, in contrast to the single previous report of cubic $La_{0.531}K_{0.469}TiO_3$, in which not all of the alkali metal was incorporated into the structure.[23]

The sintering of cold-pressed pellets of $La_{1-y}K_yTiO_3$ and $La_{0.5}K_{0.5}Ti_{1-z}Nb_zO_3$ compositions at 1350 °C under a H_2/N_2 (5%) atmosphere yielded ceramics with measured densities higher than 90% of the values expected from structural analysis (Table S12, ESI†), and SEM imaging showed the pellets to have minimal porosity (Fig. S6, ESI†).

The temperature dependences of the thermal conductivity for doped $La_{1-y}K_yTiO_3$ and $La_{0.5}K_{0.5}Ti_{1-z}Nb_zO_3$ compositions are shown in Fig. 6a. These materials exhibit low phonon-glass thermal conductivities comparable to that of undoped $La_{0.5}K_{0.5}TiO_3$ despite possessing electron carrier concentrations, determined from nominal compositions, which lie within the range expected for heavily doped semiconductors (10^{19} to 10^{21} cm^{-3}). The thermal conductivities have magnitudes of 2.45(12)–2.65(13) W m^{-1} K^{-1} at room temperature and 2.45(12)–2.80(15) W m^{-1} K^{-1} at 850 K and have a temperature dependence like κ_{min} determined from eqn (3). In contrast to the thermal conductivities of $La_{1-y}K_yTiO_3$ and $La_{0.5}K_{0.5}Ti_{1-z}Nb_zO_3$ which show no correlation with doping, the electronic conductivities and Seebeck coefficients display a strong doping dependence shown in Fig. 6b and c. In $La_{0.5}K_{0.5}Ti_{1-z}Nb_zO_3$, peak conductivities increase from 180(9) to 212(10) S cm^{-1} at 600 K for $z = 0.05$ and 0.1 respectively, whereas the peak values of σ in $La_{1-y}K_yTiO_3$ increase from 230(11) S cm^{-1} for $y = 0.45$ to 315(16) S cm^{-1} for $y = 0.4$ at 500 K, associated with increasing carrier concentration. The observed temperature dependencies of both σ and S for all compositions are similar to many doped titanate thermoelectrics reported in the literature.[40,42,46,47] Maxima in σ are observed between 500–600 K and are associated with increased resistance from acceptor-based phases which are localised to the grain boundaries.[48] The negative values of S indicate electron doping of predominantly n-type carriers within all compositions, and both A and B site doped materials exhibit decreasing $|S|$ with increasing carrier concentration which is expected for metals or parabolic band semiconductors through eqn (8)

$$S = \frac{8\pi^2 k_B^2}{3eh^2} m^* T \left(\frac{\pi}{3n}\right)^{2/3} \quad (8)$$

where h is Planck's constant, e is elementary charge, m^* is the carrier effective mass and n is the carrier concentration.[3] For $La_{0.55}K_{0.45}TiO_3$ and $La_{0.5}K_{0.5}Ti_{0.9}Nb_{0.1}O_3$, which nominally have the same n, almost identical conductivities of ≈210(10) S cm^{-1} are observed at 600 K. Interestingly for these particular compositions, $|S|$ is considerably higher for $La_{0.55}K_{0.45}TiO_3$ than for $La_{0.5}K_{0.5}Ti_{0.9}Nb_{0.1}O_3$, with values of −161(8) and −132(7) μV K^{-1} at 600 K respectively, and $|S|$ of $La_{0.6}K_{0.4}TiO_3$ is still higher than that of $La_{0.5}K_{0.5}Ti_{0.9}Nb_{0.1}O_3$ despite having a higher nominal carrier concentration. As $La_{0.55}K_{0.45}TiO_3$ and $La_{0.5}K_{0.5}Ti_{0.9}Nb_{0.1}O_3$ both have the same n but a larger $|S|$ is observed experimentally for $La_{0.55}K_{0.45}TiO_3$, from the relationship shown in eqn (8) this indicates that a higher m^* is achieved through the A site doping of $La_{1-y}K_yTiO_3$ compared to B site doping through $La_{0.5}K_{0.5}Ti_{1-z}Nb_zO_3$. This shows how the slight differences in the crystal structures of $La_{1-y}K_yTiO_3$ and $La_{0.5}K_{0.5}Ti_{1-z}Nb_zO_3$ can significantly influence the electronic properties. In general, 3d–2p orbital overlap in these perovskites is maximised through shorter bonding and/or tilt angles that approach 0°.[49] In $La_{0.5}K_{0.5}Ti_{1-z}Nb_zO_3$ the Nb^{5+} substitution retains the linear Ti–O–Ti bonding of the cubic ($Pm\bar{3}m$) structure (Table S11, ESI†). This maximises band dispersion and therefore σ, but leads to a lower m^* which supports the decreased $|S|$ observed experimentally for $La_{0.5}K_{0.5}Ti_{1-z}Nb_zO_3$. In contrast, the change of symmetry to $R\bar{3}c$ in $La_{1-y}K_yTiO_3$ reduces the orbital overlap through octahedral tilting which reduces band dispersion yielding a larger m^* and is the reason that higher $|S|$ values are observed for $La_{1-y}K_yTiO_3$ compared to $La_{0.5}K_{0.5}Ti_{1-z}Nb_zO_3$. The decrease in σ that a larger m^* is expected to bring about is offset by the increased overlap between neighbouring Ti 3d-t_{2g} orbitals in the smaller, more distorted cell of $La_{1-y}K_yTiO_3$ which accounts for the closely matched conductivities observed for $La_{0.55}K_{0.45}TiO_3$ and $La_{0.5}K_{0.5}Ti_{0.9}Nb_{0.1}O_3$.[42,50] Using the additional data available from the previous report of $La_{0.5}Na_{0.5}Ti_{1-x}Nb_xO_3$,[8] it is possible to observe the relationship

Table 2 Results of ICP-OES measurements on $La_{1-y}K_yTiO_3$ and $La_{0.5}K_{0.5}Ti_{1-z}Nb_zO_3$ materials. Values are normalised to titanium and compared against the nominal expected compositions. Metal contents were corrected by analysing metal solutions of known concentrations both separately and combined. Correction factors are La = 1.01, K = 1.10, Ti = 1.00 and Nb = 1.00. Absolute errors are shown

Nominal composition	La	K	Ti	Nb
$La_{0.5}K_{0.5}TiO_3$	0.518(3)	0.507(5)	1.000(5)	—
$La_{0.55}K_{0.45}TiO_3$	0.556(3)	0.445(2)	1.000(5)	—
$La_{0.6}K_{0.4}TiO_3$	0.608(3)	0.413(2)	1.000(7)	—
$La_{0.5}K_{0.5}Ti_{0.95}Nb_{0.05}O_3$	0.505(2)	0.493(4)	0.950(3)	0.0487(1)
$La_{0.5}K_{0.5}Ti_{0.9}Nb_{0.1}O_3$	0.507(7)	0.469(2)	0.900(6)	0.0981(1)

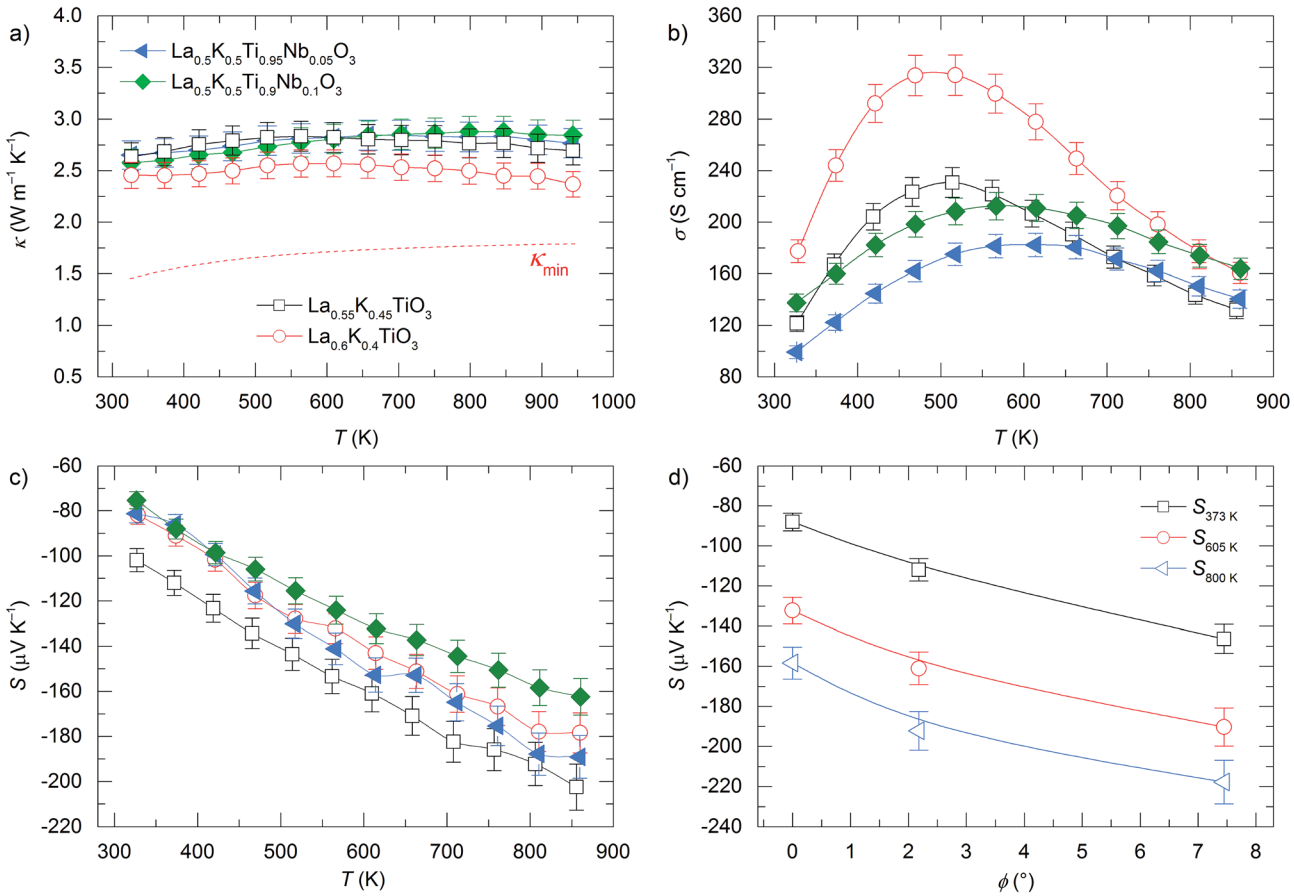

Fig. 6 Temperature dependence of (a) thermal conductivity (κ), (b) electronic conductivity (σ), and (c) Seebeck coefficient (S) for A site ($La_{1-y}K_yTiO_3$, $y = 0.45$ and 0.4) and B site ($La_{0.5}K_{0.5}Ti_{1-z}Nb_zO_3$, $z = 0.05$ and 0.1) doped compositions of $La_{0.5}K_{0.5}TiO_3$. Dependence of S as a function of tilt angle (ϕ) at different temperatures is shown in (d) using three materials that have the same nominal carrier concentration: $La_{0.5}K_{0.5}Ti_{0.9}Nb_{0.1}O_3$ ($\phi = 0°$) and $La_{0.55}K_{0.45}TiO_3$ ($\phi = 2.18(1)°$) from this study, and $La_{0.5}Na_{0.5}Ti_{0.9}Nb_{0.1}O_3$ ($\phi = 7.45(3)°$) which was taken from a recent study of PGEC $La_{0.5}Na_{0.5}Ti_{1-x}Nb_xO_3$ materials with $R\bar{3}c$ symmetry.[8]

between $|S|$ and octahedral tilt angle, which is plotted in Fig. 6d for compositions with the same nominal carrier concentration and further highlights the effects of tilting on band dispersions discussed above. $La_{0.5}K_{0.5}Ti_{0.9}Nb_{0.1}O_3$ is cubic ($Pm\bar{3}m$) with zero tilt, while both $La_{0.55}K_{0.45}TiO_3$ and $La_{0.5}Na_{0.5}Ti_{0.9}Nb_{0.1}O_3$ are rhombohedral ($R\bar{3}c$) with tilt angles of 2.18(1)° and 7.45(3)° respectively. The magnitude of $|S|$ increases with increasing tilt angle at all temperatures with a $\approx$60 μV K^{-1} difference between $La_{0.5}K_{0.5}Ti_{0.9}Nb_{0.1}O_3$ and $La_{0.5}Na_{0.5}Ti_{0.9}Nb_{0.1}O_3$ due to increased m^* as a result of reduced orbital overlap brought about by octahedral tilting. In contrast to the clear relationship between $|S|$ and the tilt angle, similar magnitudes of σ are observed for these materials with the same nominal carrier concentration. From this it is clear that despite targeting high carrier mobility by tuning the symmetry of the unit cell to maximise band dispersions in the zero-tilt structure of $La_{0.5}K_{0.5}TiO_3$, the optimisation of σ is far more complex and depends significantly on the processing conditions of the measured ceramics with extrinsic factors such as grain boundary resistance ultimately dominating σ.[42,48] The Seebeck coefficient, measured at zero current transport, should be insensitive to grain boundary effects and exhibits a clear correlation to the octahedral tilt angle.

As a result of the improved $|S|$ values observed for $La_{1-y}K_yTiO_3$ significant differences are observed between the power factors of the A and B site doped materials as shown in Fig. 7a. Enhancements in σ, particularly at low temperatures, alongside the increased m^* and $|S|$ in $La_{1-y}K_yTiO_3$ result in a power factors of 0.58(5) mW m^{-1} K^{-2} at 600 K compared to 0.39(3) mW m^{-1} K^{-2} in $La_{0.5}K_{0.5}Ti_{1-z}Nb_zO_3$. The observation of improved power factors in titanate perovskite thermoelectrics with smaller, more-distorted unit cells is commonplace; $S^2\sigma$ was enhanced with increasing values of x in the solid solution $Ba_{0.9-x}Sr_xLa_{0.1}TiO_3$,[51] and the largest $S^2\sigma$ values were achieved for the smallest lanthanides studied in $Sr_{0.9}R_{0.1}TiO_{3-\delta}$.[42] In this study, when considering both σ and S, the electronic transport is improved in $La_{1-y}K_yTiO_3$ compositions ($y = 0.45$ and 0.4) across the entire measured temperature range compared to B site doped $La_{0.5}K_{0.5}Ti_{1-z}Nb_zO_3$ as shown in Fig. 7a and is ascribed to the improved Seebeck coefficients which result from lower band dispersions and higher m^* in the more distorted structures of $La_{1-y}K_yTiO_3$. The power factors of the $La_{1-y}K_yTiO_3$ series are comparable to those of $La_{0.5}Na_{0.5}Ti_{1-x}Nb_xO_3$ reported previously.[8]

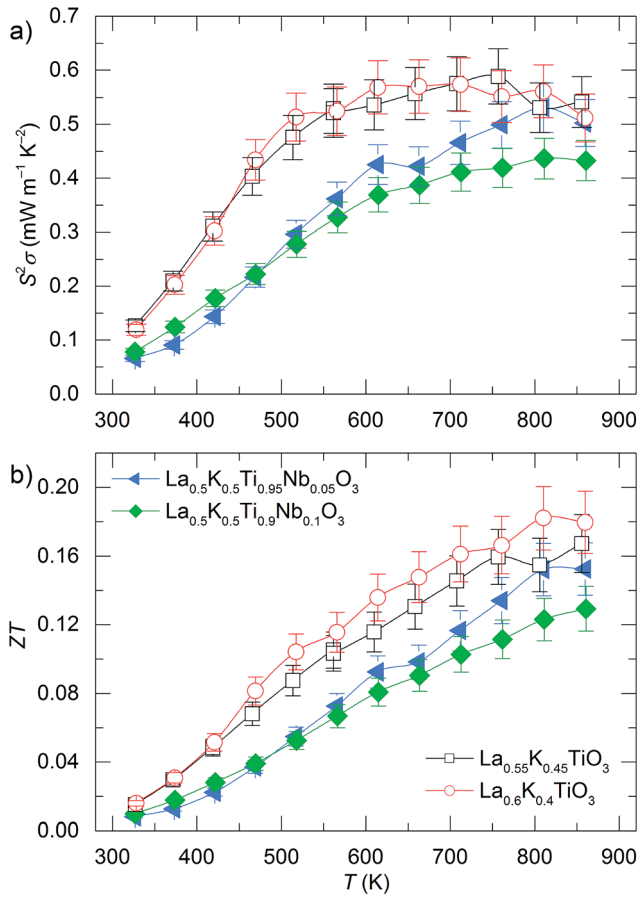

Fig. 7 Temperature dependence of (a) thermoelectric power factors ($S^2\sigma$) and (b) thermoelectric figures of merit (ZT) for $La_{1-y}K_yTiO_3$ and $La_{0.5}K_{0.5}Ti_{1-z}Nb_zO_3$ compositions.

Even though higher power factors are achieved for $La_{1-y}K_yTiO_3$ compared against $La_{0.5}K_{0.5}Ti_{1-z}Nb_zO_3$, both series retain the same glass-like thermal conductivity of the undoped $La_{0.5}K_{0.5}TiO_3$ parent and the electronic contribution to the thermal conductivity (κ_{elec}) is no larger than 12% for all samples (Fig. S11, ESI†). This highlights the weak correlation between electronic and thermal transport within these materials, properties that are usually very strongly coupled in titanate thermoelectrics with κ_{elec} contributing $\approx$25% of the total thermal conductivity in similarly doped $Sr_{1-x}La_xTiO_{3-\delta}$,[15] and again demonstrates the advantage of utilising cation mass disorder to control κ_{latt} which remains the dominant contributor to κ in these materials.

Peak ZT values of $\approx$0.18 are observed at 800 K in $La_{1-y}K_yTiO_3$ compositions and the figures of merit increase with temperature for all materials, as shown in Fig. 7b. These are slightly lower than the highest values obtained previously from $La_{0.5}Na_{0.5}Ti_{1-x}Nb_xO_3$ and result from the combination of comparable power factors and slightly higher thermal conductivities in $La_{1-y}K_yTiO_3$ and $La_{0.5}K_{0.5}Ti_{1-z}Nb_zO_3$. The improved performance of A site doped $La_{1-y}K_yTiO_3$ over B site doped $La_{0.5}K_{0.5}Ti_{1-z}Nb_zO_3$ is clear, not only in peak ZT but also for the entire measurement range. This increased figure of merit is attributed to the enhanced power factors (Fig. 7a) which originate from decreased band dispersions in more distorted $La_{1-y}K_yTiO_3$ materials. At all temperatures, the ZT values of $La_{1-y}K_yTiO_3$ are typically 20–50% higher than those of $La_{0.5}K_{0.5}Ti_{1-z}Nb_zO_3$ with the largest differences in the intermediate temperature range (350–700 K). As a result of this, the average energy conversion efficiencies (ε_{ave}) of $La_{1-y}K_yTiO_3$ are a respectable 1.39–1.59%, for $y = 0.45$ and 0.4 respectively, compared against 0.093–0.097% for in $La_{0.5}K_{0.5}Ti_{1-z}Nb_zO_3$ respectively, when evaluated through eqn (9) over the temperature ranges applicable to the recovery of waste heat from automotive exhausts.[4]

$$\varepsilon_{ave} = \frac{\frac{T_H - T_C}{T_H}\int_{T_C}^{T_H}\frac{\sqrt{ZT+1}-1}{\sqrt{ZT+1}+(T_C/T_H)}dT}{T_H - T_C} \quad (9)$$

The large difference in efficiencies between $La_{1-y}K_yTiO_3$ and $La_{0.5}K_{0.5}Ti_{1-z}Nb_zO_3$ is due to the increased figures of merit across the temperature range 350–700 K, and not due to the highest peak value. The importance of $ZT_{average}$, particularly for application temperature ranges, is frequently overlooked when searching for new peak ZT materials.

Conclusions

This work presents the study of a new solid solution between phonon-glass $La_{0.5}Na_{0.5}TiO_3$ ($R\bar{3}c$) and $La_{0.5}K_{0.5}TiO_3$ ($Pm\bar{3}m$). It is possible to tune the cation size on the A site in order to target the cubic structure with linear Ti–O–Ti bonding that is associated with the high electronic conductivity of $SrTiO_3$ based thermoelectrics. $La_{0.5}K_{0.5}TiO_3$ is the first reported cubic phonon-glass titanate thermoelectric. The phonon-glass thermal conductivity results from localised phonon interactions caused by the disordered distribution of high mass contrast La^{3+} and K^+. Electronic carriers can be introduced through either A or B site doping in $La_{1-y}K_yTiO_3$ and $La_{0.5}K_{0.5}Ti_{1-z}Nb_zO_3$, respectively. The A site doping through $La_{1-y}K_yTiO_3$ leads to larger power factors and a higher overall ZT performance compared to B site doped $La_{0.5}K_{0.5}Ti_{1-z}Nb_zO_3$. We find that the electronic conductivity is dominated by extrinsic effects such as grain boundary resistance despite band dispersions being optimised through the cubic symmetry of $La_{0.5}K_{0.5}TiO_3$. The Seebeck coefficient is unaffected by the extrinsic factors and this performance gain is associated with the more distorted and lower symmetry structures of $La_{1-y}K_yTiO_3$ ($R\bar{3}c$) compositions which decrease band dispersion and lead to higher effective masses and Seebeck coefficients compared with $La_{0.5}K_{0.5}Ti_{1-z}Nb_zO_3$ ($Pm\bar{3}m$). Phonon-glass thermal conductivities are retained for both A and B site doped materials providing a further example of how intrinsic cation mass disorder can minimise the correlation between the usually strongly coupled thermal and electronic transport in perovskites and yield PGEC behaviour in a cubic titanate thermoelectric. The control of power factors through the distortion of the unit cell could provide guidance in the choice of future target materials, such as combining high mass contrast

compositions with smaller cations to target improved electronic transport (*e.g.* $Ln_{0.5}A_{0.5}TiO_3$ where A = Na^+/K^+, and Ln = Dy^{3+}/Ho^{3+}).

Conflicts of interest

There are no conflicts to declare.

Acknowledgements

We thank EPSRC for funding under EP/N004884. We thank the Materials Chemistry Consortium (EPSRC: EP/L000202) for provision of computer time on ARCHER UK National Supercomputing Service. We thank Diamond Light Source and ISIS for provision of beamtime, and Claire Murray, Sarah Day and Paul Henry for assistance on the I11 and HRPD instruments. Marco Zanella is thanked for measurement of SEM images.

Notes and references

1 S. Hebert, D. Berthebaud, R. Daou, Y. Breard, D. Pelloquin, E. Guilmeau, F. Gascoin, O. Lebedev and A. Maignan, *J. Phys.: Condens. Matter*, 2016, **28**, 013001.
2 T. M. Tritt and M. A. Subramanian, *MRS Bull.*, 2011, **31**, 188–198.
3 G. J. Snyder and E. S. Toberer, *Nat. Mater.*, 2008, **7**, 105–114.
4 J. Yang and T. Caillat, *MRS Bull.*, 2011, **31**, 224–229.
5 G. A. Slack, *CRC Handbook of Thermoelectrics*, CRC, Boca Raton, 1995.
6 M. Christensen, A. B. Abrahamsen, N. B. Christensen, F. Juranyi, N. H. Andersen, K. Lefmann, J. Andreasson, C. R. Bahl and B. B. Iversen, *Nat. Mater.*, 2008, **7**, 811–815.
7 M. M. Koza, M. R. Johnson, R. Viennois, H. Mutka, L. Girard and D. Ravot, *Nat. Mater.*, 2008, **7**, 805–810.
8 L. M. Daniels, S. N. Savvin, M. J. Pitcher, M. S. Dyer, J. B. Claridge, S. Ling, B. Slater, F. Cora, J. Alaria and M. J. Rosseinsky, *Energy Environ. Sci.*, 2017, **10**, 1917–1922.
9 S. LeBlanc, S. K. Yee, M. L. Scullin, C. Dames and K. E. Goodson, *Renewable Sustainable Energy Rev.*, 2014, **32**, 313–327.
10 R. Boston, W. L. Schmidt, G. D. Lewin, A. C. Iyasara, Z. Lu, H. Zhang, D. C. Sinclair and I. M. Reaney, *Chem. Mater.*, 2016, **29**, 265–280.
11 J. W. Fergus, *J. Eur. Ceram. Soc.*, 2012, **32**, 525–540.
12 J. Wang, B.-Y. Zhang, H.-J. Kang, Y. Li, X. Yaer, J.-F. Li, Q. Tan, S. Zhang, G.-H. Fan, C.-Y. Liu, L. Miao, D. Nan, T.-M. Wang and L.-D. Zhao, *Nano Energy*, 2017, **35**, 387–395.
13 K. Shirai and K. Yamanaka, *J. Appl. Phys.*, 2013, **113**, 053705.
14 S. Ohta, T. Nomura, H. Ohta, M. Hirano, H. Hosono and K. Koumoto, *Appl. Phys. Lett.*, 2005, **87**, 092108.
15 T. Okuda, K. Nakanishi, S. Miyasaka and Y. Tokura, *Phys. Rev. B: Condens. Matter Mater. Phys.*, 2001, **63**, 113104.
16 Y. Wang, K. Fujinami, R. Zhang, C. Wan, N. Wang, Y. Ba and K. Koumoto, *Appl. Phys. Express*, 2010, **3**, 031101.
17 R. Garg, A. Senyshyn, H. Boysen and R. Ranjan, *J. Phys.: Condens. Matter*, 2008, **20**, 505215.
18 V. M. Goldschmidt, *Naturwissenschaften*, 1926, **14**, 477–485.
19 R. H. Mitchell, *Perovskites: Modern and Ancient*, Almaz Press Inc., Thunder Bay, ON, Canada, 2002.
20 R. D. Shannon, *Acta Crystallogr., Sect. A: Cryst. Phys., Diffr., Theor. Gen. Crystallogr.*, 1976, **32**, 751–767.
21 W. Zhao, G. Zhu, W. Zhao, T. Lin, F. Xu and F. Huang, *Dalton Trans.*, 2015, **44**, 18665–18670.
22 J.-P. Miao, Z. Lü, L.-P. Li, F.-L. Ning, Z.-G. Liu, X.-Q. Huang, Y. Sui, Z.-N. Qian and W.-H. Su, *J. Alloys Compd.*, 2005, **387**, 287–291.
23 J. Brous, I. Fankuchen and E. Banks, *Acta Crystallogr.*, 1953, **6**, 67–70.
24 A. A. Coelho, *J. Appl. Crystallogr.*, 2000, **33**, 899–908.
25 G. V. Chester and A. Thellung, *Proc. Phys. Soc., London*, 1961, **77**, 1005–1013.
26 J. Hutter, M. Iannuzzi, F. Schiffmann and J. VandeVondele, *Wiley Interdiscip. Rev.: Comput. Mol. Sci.*, 2014, **4**, 15–25.
27 J. P. Perdew, K. Burke and M. Ernzerhof, *Phys. Rev. Lett.*, 1996, **77**, 3865.
28 J. VandeVondele, M. Krack, F. Mohamed, M. Parrinello, T. Chassaing and J. Hutter, *Comput. Phys. Commun.*, 2005, **167**, 103–128.
29 S. Godecker, M. Teter and J. Hutter, *Phys. Rev. B: Condens. Matter Mater. Phys.*, 1996, **54**, 1703.
30 M. Krack, *Theor. Chem. Acc.*, 2005, **114**, 145–152.
31 C. Adamo and V. Barone, *J. Chem. Phys.*, 1999, **110**, 6158–6170.
32 R. Dovesi, R. Orlando, A. Erba, C. M. Zicovich-Wilson, B. Civalleri, S. Casassa, L. Maschio, M. Ferrabone, M. De La Pierre, P. D'Arco, Y. Noël, M. Causà, M. Rérat and B. Kirtman, *Int. J. Quantum Chem.*, 2014, **114**, 1287–1317.
33 A. M. Glazer, *Acta Crystallogr., Sect. B: Struct. Crystallogr. Cryst. Chem.*, 1972, **28**, 3384–3392.
34 H. D. Megaw and C. N. W. Darlington, *Acta Crystallogr., Sect. A: Cryst. Phys., Diffr., Theor. Gen. Crystallogr.*, 1975, **31**, 161–173.
35 K. Robinson, G. V. Gibbs and P. H. Ribbe, *Science*, 1971, **172**, 567–570.
36 Y. A. Abramov, V. G. Tsirelson, V. E. Zavodnik, S. A. Ivanoc and I. D. Brown, *Acta Crystallogr., Sect. B: Struct. Sci.*, 1995, **51**, 942–951.
37 E. S. Toberer, A. Zevalkink and G. J. Snyder, *J. Mater. Chem.*, 2011, **21**, 15843–15852.
38 D. G. Cahill, S. K. Watson and R. O. Pohl, *Phys. Rev. B: Condens. Matter Mater. Phys.*, 1992, **46**, 6131–6140.
39 W. Kaiser and R. Zurek, *Phys. Lett.*, 1966, **23**, 668.
40 S. R. Popuri, A. J. M. Scott, R. A. Downie, M. A. Hall, E. Suard, R. Decourt, M. Pollet and J. W. G. Bos, *RSC Adv.*, 2014, **4**, 33720–33723.
41 S. Bhattacharya, A. Mehdizadeh Dehkordi, S. Tennakoon, R. Adebisi, J. R. Gladden, T. Darroudi, H. N. Alshareef and T. M. Tritt, *J. Appl. Phys.*, 2014, **115**, 223712.
42 A. V. Kovalevsky, A. A. Yaremchenko, S. Populoh, P. Thiel, D. P. Fagg, A. Weidenkaff and J. R. Frade, *Phys. Chem. Chem. Phys.*, 2014, **16**, 26946–26954.
43 L. Feng, T. Shiga and J. Shiomi, *Appl. Phys. Express*, 2015, **8**, 071501.

44 T. M. Tritt, *Thermal Conductivity: Theory, Properties and Applications*, Kluwer Academic, New York, USA, 2004.
45 A. A. Yaremchenko, S. Populoh, S. G. Patrício, J. Macías, P. Thiel, D. P. Fagg, A. Weidenkaff, J. R. Frade and A. V. Kovalevsky, *Chem. Mater.*, 2015, **27**, 4995–5006.
46 B. Zhang, J. Wang, T. Zou, S. Zhang, X. Yaer, N. Ding, C. Liu, L. Miao, Y. Li and Y. Wu, *J. Mater. Chem. C*, 2015, **3**, 11406–11411.
47 T. Q. Thong, L. T. T. Huong and N. T. Tinh, *Mater. Trans.*, 2015, **56**, 1365–1369.
48 R. Moos and K. H. Härdtl, *J. Appl. Phys.*, 1996, **80**, 393–400.
49 A. Cammarata and J. M. Rondinelli, *J. Chem. Phys.*, 2014, **141**, 114704.
50 J. B. Goodenough, *J. Appl. Phys.*, 1966, **37**, 1415–1422.
51 H. Muta, K. Kurosaki and S. Yamanaka, *J. Alloys Compd.*, 2004, **368**, 22–24.